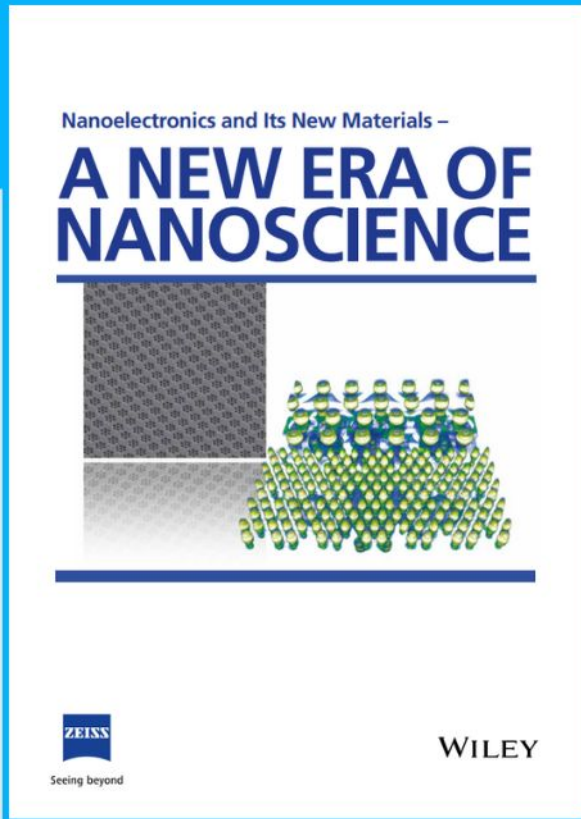




# Nanoelectronics and Its New Materials – A NEW ERA OF NANOSCIENCE



**Discover the recent advances in electronics research and fundamental nanoscience.**

Nanotechnology has become the driving force behind breakthroughs in engineering, materials science, physics, chemistry, and biological sciences. In this compendium, we delve into a wide range of novel applications that highlight recent advances in electronics research and fundamental nanoscience. From surface analysis and defect detection to tailored optical functionality and transparent nanowire electrodes, this eBook covers key topics that will revolutionize the future of electronics.

To get your hands on this valuable resource and unleash the power of nanotechnology, simply download the eBook now. Stay ahead of the curve and embrace the future of electronics with nanoscience as your guide.



Seeing beyond

**WILEY**

# Impact of Minor Alloy Components on the Electrocapillarity and Electrochemistry of Liquid Metal Fractals

Ruohan Yu, Jialuo Han, Yuan Chi, Jiewei Zheng, Richard Fuchs, Mohammad B. Ghasemian, Md. Arifur Rahim, Shi-Yang Tang, Guangzhao Mao,\* Kourosh Kalantar-Zadeh,\* and Jianbo Tang\*

Exploring and controlling surface tension-driven phenomena in liquid metals may lead to unprecedented possibilities for next-generation microfluidics, electronics, catalysis, and materials synthesis. In pursuit of these goals, the impact of minor constituents within liquid alloys is largely overlooked. Herein, it is shown that the presence of a fraction of solute metals such as tin, bismuth, and zinc in liquid gallium can significantly influence their electrocapillarity and electrochemistry. The instability-driven fractal formation of liquid alloy droplets is investigated with different solutes and reveals the formation of distinctive non-branched droplets, unstable fractals, and stable fractal modes under controlled voltage and alkaline solution conditions. In their individually unique fractal morphology diagrams, different liquid alloys demonstrate significantly shifted voltage thresholds in transition between the three fractal modes, depending on the choice of the solute metal. Surface tension measurements, cycle voltammetry and surface compositional characterizations provide strong evidence that the minor alloy components drastically alter the surface tension, surface electrochemical oxidation, and oxide dissolution processes that govern the droplet deformation and instability dynamics. The findings that minor components are able to regulate liquid alloys' surface tensions, surface element distributions and electrochemical activities offer great promises for harnessing the tunability and functionality of liquid metals.

## 1. Introduction

Liquid metals, a promising family of functional materials that combine the physicochemical properties of metals and fluids,<sup>[1]</sup> are responsive to various forms of external stimuli.<sup>[2]</sup> Consequently, versatile control strategies can be implemented by leveraging liquid metals' multi-stimuli responsiveness.<sup>[2a,3]</sup> As a result, liquid metals have been increasingly employed as intelligent materials in next-generation microfluidics,<sup>[4]</sup> reconfigurable electronics,<sup>[5]</sup> soft or liquid robots,<sup>[6]</sup> liquid catalysis,<sup>[7]</sup> and biomedical applications.<sup>[8]</sup> Gallium (Ga) and its alloys are now the most frequently investigated liquid metals due to their low melting temperature, low vapor pressure, and negligible toxicity. Specifically, these dense metallic liquids are characterized by their exceedingly high surface tension. To provide context, it is worth noting that the surface tension of liquid Ga ( $\approx 500 \text{ mN m}^{-1}$ ) is  $\approx 7$  times higher than that of water.<sup>[9]</sup> The high surface tension of liquid metals is critical for their handling, processing,

R. Yu, Y. Chi, J. Zheng, R. Fuchs, M. B. Ghasemian, M. A. Rahim, G. Mao, K. Kalantar-Zadeh, J. Tang  
School of Chemical Engineering  
University of New South Wales (UNSW)  
Kensington, NSW 2052, Australia  
E-mail: guangzhao.mao@unsw.edu.au;  
kourosh.kalantarzadeh@sydney.edu.au; jianbo.tang@unsw.edu.au  
J. Han  
CSIRO Manufacturing  
Bag 10, Clayton South, Victoria 3169, Australia

M. B. Ghasemian, M. A. Rahim, K. Kalantar-Zadeh  
School of Chemical and Biomolecular Engineering  
University of Sydney  
Darlington, NSW 2008, Australia  
S.-Y. Tang  
Department of Electronic  
Electrical and Systems Engineering  
University of Birmingham  
Edgbaston, Birmingham B15 2TT, UK

 The ORCID identification number(s) for the author(s) of this article can be found under <https://doi.org/10.1002/adfm.202301348>

© 2023 The Authors. Advanced Functional Materials published by Wiley-VCH GmbH. This is an open access article under the terms of the Creative Commons Attribution License, which permits use, distribution and reproduction in any medium, provided the original work is properly cited.

DOI: 10.1002/adfm.202301348

and ultimately liquid metal-based synthesis and applications. One of the most distinctive signatures of the surface tension of liquid metals is its tunability.<sup>[10]</sup> Liquid metals' surface tension can be regulated from its original high value to near zero using chemical or physical means, and in particular electrochemical methods.<sup>[11]</sup>

Electric-field-induced surface tension alteration, referred to as the electrocapillary effect,<sup>[10a]</sup> is an effective and reversible mechanism widely applied for controlling the motion and deformation of liquid metal objects.<sup>[6,12]</sup> To date, the realization of on-demand control of liquid metal motion and deformation has led to many intelligent microfluidic systems and functional devices including smart pumps,<sup>[12b,13]</sup> actuators,<sup>[6,14]</sup> and antennas,<sup>[5a,15]</sup> and enabled novel material synthesis strategies.<sup>[16]</sup>

High-surface tension liquid metals naturally adapt to spherical or near-spherical shapes to minimize their surface energy. When subjected to an external electrical field (normally in an electrolyte environment), liquid metals' surface tension decreases following Lippman's theory.<sup>[17]</sup> For Ga-based liquid metals, an electrochemical oxidation process takes place simultaneously, which further affects their apparent surface tension. As a result, the liquid metals can spread and create branches, leading to the so-called fingering instability and the formation of fractals.<sup>[18]</sup> Therefore, the fractal formation behaviors are indicative of the surface tension change of the liquid metals and the impact of electrochemical processes on their surface behaviors. However, it is important to consider that under strongly oxidizing conditions, the influence of surface oxidation can become dominant and liquid metals' surface tension may not be accurately predicted by Lippman's theory. Fractals are classical systems for studying surface phenomena and instabilities of both non-metallic liquids<sup>[18,19]</sup> and liquid metals.<sup>[11a,20]</sup> Previous reports on liquid metal fractals have mainly focused on the influence of extrinsic parameters such as applied voltage, liquid metal volume, and electrolyte type.<sup>[11a,20b,c]</sup> However, the studies of various intrinsic parameters, including the effects of solutes of other metals, have been overlooked.

As an intrinsic characteristic, the composition of liquid metals governs many of their properties, including their surface tension. Evidence shows that it is possible to cause considerable changes to the properties, especially the surface characteristics, of a liquid metal (solvent) by adding a small amount of secondary metal (solute).<sup>[21]</sup> In a multi-component liquid metal system, the surface elemental composition is usually driven by thermodynamic energetics, not necessarily their relative nominal ratios. As a result, a minor component added to liquid metals can have a significant surface presence, leading to compositional and structural differences between the surface and bulk.<sup>[18,22]</sup> Such surface-specific element distributions result in surprising surface oxidation,<sup>[16c]</sup> phase transition,<sup>[18,23]</sup> catalytic activity,<sup>[7]</sup> and rheological behaviors<sup>[24]</sup> in liquid metals. However, to date, the influence of minor (dilute) alloy components on the electrocapillary and electrochemical behaviors in liquid metal systems has not been examined. Additionally, in the presence of an external electric field, the elemental distribution within the liquid metal system may be further affected, apart from the changes in their surface tension and surface electrochemistry.

Here, we investigated the fractal formation behaviors in liquid Ga and dilute tin-Ga (SnGa), bismuth-Ga (BiGa), and zinc-Ga (ZnGa) liquid alloys to shed light on how the low-ratio sec-

ondary metals Sn, Bi, and Zn influence their electrocapillary and surface electrochemical processes of Ga-based liquid metals. The liquid metal fractals were obtained by applying a positive DC voltage on liquid metal droplets immersed in a sodium hydroxide (NaOH) environment. We observed distinct fractal formation behaviors arising from the liquid metals' composition difference, which imply their distinct surface states and activities. Surface tension measurements, electrochemical tests, and surface composition/structure characterizations were performed to explain our experimental observations. It was found that despite their low contents, the secondary metals could significantly change the liquid metals' response to the external electrical stimulus through affecting their surface tension and surface oxidation. As a result, different liquid metal deformation modes and fractal morphologies were generated. In addition, an interesting electrical-field-induced element redistribution was observed in the ZnGa alloy. Our results highlight the important role of minor components in liquid metal systems in terms of affecting their surface tension, surface electrochemistry, as well as surface element distribution.

## 2. Results and Discussion

### 2.1. Liquid Metal Fractals

The experimental setups used for the formation and observation of liquid metal fractals are illustrated in **Figure 1**. To investigate the influence of secondary metals (at dilute ratios) on the fractal formation behaviors, three Ga-based binary alloys Ga<sub>0.997</sub>Bi<sub>0.003</sub>, Ga<sub>0.983</sub>Sn<sub>0.017</sub>, and Ga<sub>0.961</sub>Zn<sub>0.039</sub> (subscripts indicate weight ratios) were tested and compared with Ga. Post transition metals Bi, Sn, Zn were chosen as the secondary metal and the ratio of each secondary metal was selected so that the melting point of the resulting alloys was close to (but sufficiently higher than) room temperature so that they could be handled as liquids and at the same time be solidified as required for further characterizations. In a typical liquid metal fractal experiment, a liquid metal droplet (14  $\mu$ L in volume) was placed in a Petri dish prefilled with NaOH solution. Before applying an external voltage, the droplet remained near spherical in the solution. Upon applying a voltage  $U$  (positive) to the liquid metal droplet, it deformed (flattened) immediately under the influence of gravity. The deformation of the droplet depended on the liquid metal composition, the magnitude of  $U$  as well as the concentration of the NaOH solution ( $c$ ), implying different interfacial activities.

For all four cases, the deformations of the liquid metal droplets were categorized into three modes based on the shape and instability of the droplets (Figure 1d–g; and Video S1–S4, Supporting Information): i) At low  $U$ , the spherical droplets flattened slightly to form a sessile pancake shape with no branch, which is here referred to as the “nonbranched droplet” mode (Mode 1). The droplets could detach from a tungsten (W) electrode during deformation, after which their spherical shape was reattained; ii) At intermediate  $U$ , interfacial instability became dominant and the liquid metal droplets flattened considerably and spread to form multiple branches, resulting in a fast surface area increase. The branches became progressively thinner toward the center of the liquid metal (where it was in contact with the W electrode), and the fractals eventually broke up into several fragments. This mode is defined as the “unstable fractal” mode (Mode 2); iii) A

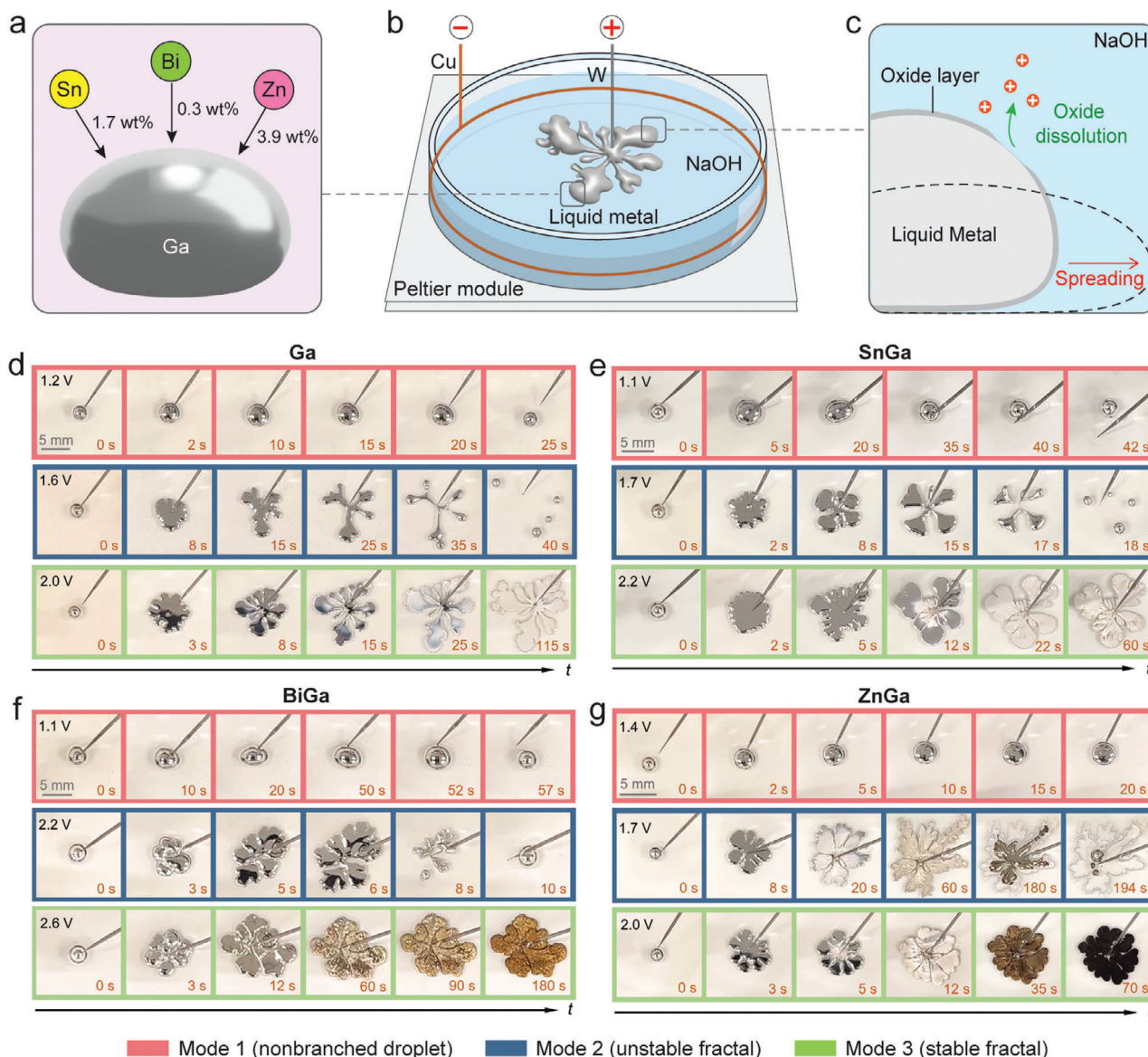


**Figure 1.** a–c) Schematic demonstration of the four Ga-based liquid metals (Ga, BiGa, SnGa, and ZnGa) investigated (a), the liquid metal fractal experimental setups (b), and surface tension-induced liquid metal deformation during fractal formation under the influence of surface oxidation and oxide dissolution (c). d–g) Comparison of shape deformations of Ga d) (Video S1, Supporting Information), SnGa e) (Video S2, Supporting Information), BiGa f) (Video S3, Supporting Information), and ZnGa g) (Video S4, Supporting Information) liquid metal droplets triggered by an external DC voltage as a function of time. The droplets' deformations were categorized into three different modes, namely the nonbranched droplet mode (Mode 1, pink outline), the unstable fractal mode (Mode 2, blue outline), and the stable fractal mode (Mode 3, green outline). The cases were conducted at  $c = 1.0 \text{ mol L}^{-1}$  for Ga, SnGa, and BiGa, and at  $c = 2.0 \text{ mol L}^{-1}$  for ZnGa. The applied  $U$ , which was varied across different liquid metal systems, was indicated in each figure.

“stable fractal” mode (Mode 3) occurs at high  $U$ , where the fractals formed by the branching liquid metal droplets were able to maintain stable shapes. In this mode, the surface of the liquid metal was observed to change its lustrous metallic color to a non-metallic dull appearance during the fractal formation process. Similar features in terms of droplet shapes and fractal modes have been observed by Eaker et al. in a different liquid metal system (eutectic GaIn alloy).<sup>[20c]</sup>

It is notable that while the three-mode categorization can be applied to all four Ga liquid metals, the transition thresholds be-

tween the low, intermediate, and high  $U$  levels were different (Figure S1, Supporting Information). In addition, the appearance of the samples in the “stable fractal” mode, which related to the liquid metal surface oxide (to be discussed later), varied between different liquid metal compositions. Both the Ga and SnGa fractals showed a silver-grey surface color, while the BiGa and ZnGa fractals became brown and dark grey, respectively. These results indicate that the secondary metal added to Ga had remarkable impacts on the electrocapillary and electrochemical behaviors of the resulting liquid alloys, despite their dilute contents.

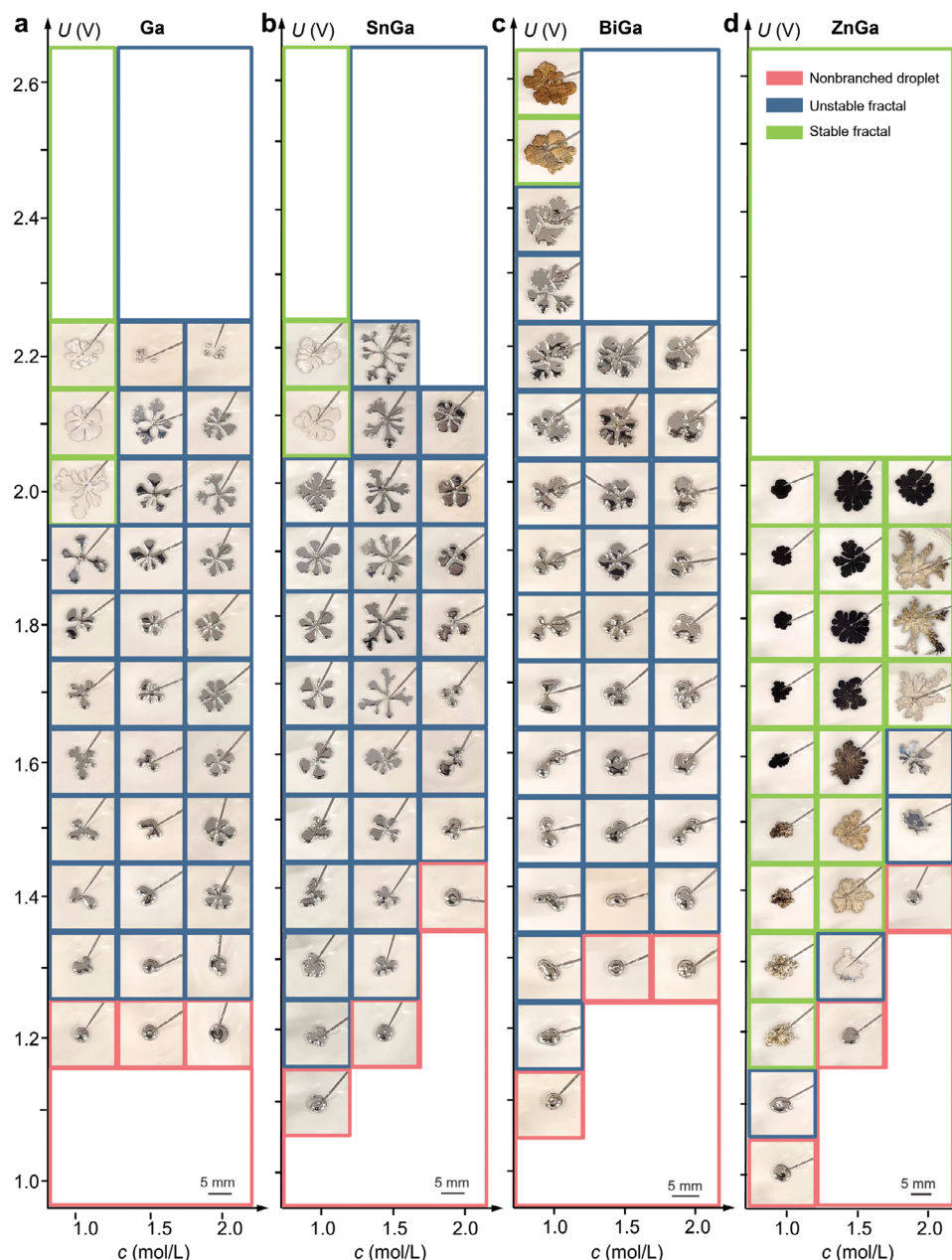


**Figure 2.** a–d) Liquid metal fractal morphology diagrams of Ga a), SnGa b), BiGa c), and ZnGa d) under different voltage,  $U$ , and NaOH concentrations,  $c$ . The morphologies represent the droplets' shapes at the maximum expansion (Mode 1 and 2) or the stable fractal state (Mode 3).

## 2.2. Liquid Metal Fractal Morphology Diagrams

The applied voltage  $U$  and the concentration of the NaOH solution  $c$ , which determined the oxidation and oxide removal rate, respectively, were found to be two critical parameters that governed the fractal formation behaviors. By varying these two parameters, a large number ( $> 120$ ) of experiments on individual droplets were performed for all four liquid metals, which allowed us to construct the liquid metal fractal morphology diagrams shown in **Figure 2**. In doing so, the snapshots of the liquid metal at the maximum expansion (largest surface area, for Mode 1 and 2) or the stable fractal state (for Mode 3) were selected and presented.

Unless otherwise specified, fresh liquid metal droplets were used for each of the experiments, as the compositions of the samples were found to change after repeated experiments (Figures S2 and S3, Supporting Information).

As shown in **Figure 2**, increasing  $U$  drove the shape transformation from Mode 1 (non-branched droplet mode) to Mode 2 and/or Mode 3, in which unstable or stable fractals emerged. The transition between the three different modes was highly dependent on the liquid metal composition, which was reflected by the distinct thresholds of  $U$  for the transition from Mode 1 to Mode 2 ( $U_{1,2}$ ) and that from Mode 2 to Mode 3 ( $U_{2,3}$ ) observed in different liquid metal systems. At fixed NaOH concentration

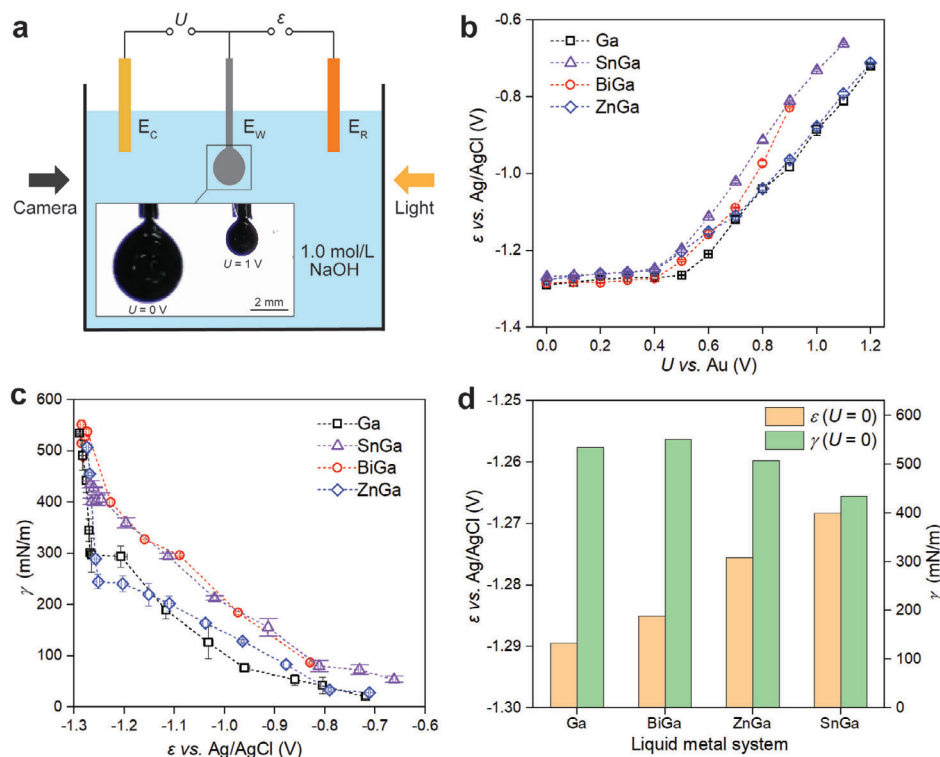


**Figure 3.** a) Schematic apparatus of surface tension measurement. The inset optical images show a BiGa liquid metal pendant drop at high and low surface tension state, respectively. b) The development of  $\epsilon$  as a function of  $U$  for different liquid metals. c) The development of surface tension  $\gamma$  as a function of  $\epsilon$  for different liquid metals. d) Comparison of  $\epsilon$  and  $\gamma$  between different liquid metals at  $U = 0$  V.

( $c = 1.0 \text{ mol L}^{-1}$ ),  $U_{1,2}$  of the SnGa, BiGa, and ZnGa droplets decreased in comparison to the Ga case. In terms of  $c$ ,  $U_{1,2}$  did not show noticeable concentration dependence for the Ga case, which, however, revealed an overall increasing trend for all three alloy samples. The threshold  $U_{2,3}$  differed considerably among the four liquid metals. Ga, BiGa, and SnGa liquid metal droplets were not able to form stable fractals (Mode 3) at high NaOH concentrations ( $c = 1.5 \text{ mol L}^{-1}$  and  $2.0 \text{ mol L}^{-1}$ ), and their fractals were unstable even at high  $U$ . By contrast, stable ZnGa fractals formed in all the three concentrations at a  $U$  as low as  $1.2 \text{ V}$  ( $c = 1.0 \text{ mol L}^{-1}$ ). As can be seen from the morphology diagrams, the ZnGa liquid metal formed stable fractals in a wide  $U$  and  $c$  range, while unstable fractals dominated the Ga, SnGa, and BiGa droplet morphology.

Considering that the ZnGa had a noticeably higher ratio than the other alloy samples, we repeated the experiment with a more diluted ZnGa alloy which contained 0.3 wt% Zn (Figures S5 and S6 and Video S5, Supporting Information). A decrease in  $U_{1,2}$  and an increase in  $U_{2,3}$  were found at this reduced Zn ratio, leading to an expanded unstable fractal region (Mode 2) in the morphology diagram. For the ZnGa cases at low NaOH concentrations ( $c = 1.0 \text{ mol L}^{-1}$ ), the stable fractals could contract noticeably after reaching their maximum spreading (Figure S4 and Video S6, Supporting Information). This effect was observed with both  $\text{Zn}_{0.039}\text{Ga}_{0.961}$  (when  $U \geq 1.3 \text{ V}$ ) (Figure 2) and  $\text{Zn}_{0.003}\text{Ga}_{0.997}$  (when  $U \geq 2.0 \text{ V}$ ) (Figure S6, Supporting Information), which agrees with a previous report.<sup>[20c]</sup> Such a fractal contraction behavior here was attributed to the partial surface tension recovery of the liquid metal. The surface tension recovery was thought to

result from suppression of the electrocapillary effect when a thick surface oxide layer (which acts as a dielectric barrier) was formed.

### 2.3. Electrocapillarity and Electrochemistry of Liquid Metal Surfaces

The surface tension of different liquid metals under different applied voltages  $U$  ( $c = 1.0 \text{ mol L}^{-1}$ ) was measured to explain the observed fractal formation behaviors. A pendant-drop method was used in the surface tension measurement,<sup>[12c]</sup> and the setup was illustrated in Figure 3a. The surface tension ( $\gamma$ ) of different liquid metal samples was determined based on the shape of the hanging droplets. Applying a DC voltage  $U$  between the working electrode  $E_W$  (pendent liquid metal droplets) and the counter electrode  $E_C$  altered the surface potential  $\epsilon$  between  $E_W$  and the reference electrode  $E_R$ . This was accompanied by a change in the droplet shapes (Figure S7, Supporting Information), based on which  $\gamma$  was estimated. Note that both  $U$  and  $\epsilon$  were presented to demonstrate how the applied external voltage influence the surface potential and thus the surface tension of the liquid metals. This setup showed good consistency in liquid metal surface tension measurement in comparison to the three-electrode configuration measured using an electrochemical workstation (Figure S8, Supporting Information).

It was evident from the  $\epsilon$ - $U$  curves that  $\epsilon$  rose slowly but stayed below about  $-1.25 \text{ V}$  before  $U$  reached  $0.5 \text{ V}$ . When  $U$  surpassed the point  $0.5 \text{ V}$ ,  $\epsilon$  ramped up with a large slope and the trend applied to all four liquid metals (Figure 3b). In corresponds to the

sudden shift in the  $\epsilon$ - $U$  curves, a similar transition was observed in the  $\gamma$ - $\epsilon$  curves, i.e., a steeper decrease in  $\gamma$  occurred before  $\epsilon \sim -1.25$  V, after which the decrease in surface tension slowed down (Figure 3c).

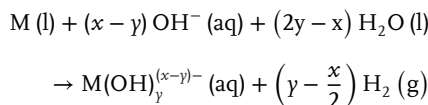
It should be noted that despite the similar trends in their  $\epsilon$ - $U$  and  $\gamma$ - $\epsilon$  curves, the four liquid metals displayed different surface properties (surface tension and interfacial potential), particularly when no external voltage was applied ( $U = 0$ ). At  $U = 0$ ,  $\epsilon$  was different from the open circuit potentials (OCPs) of the liquid metals which were measured to be close to  $-1.6$  V for all samples (Figure S9, Supporting Information), indicating a non-zero current at  $U = 0$ . As shown in Figure 3d, Ga and SnGa have the lowest and highest  $\epsilon$  among the four liquid metals, respectively. Interestingly, the surface tension  $\gamma$  of Ga was measured to be relatively high while that of SnGa was relatively low among all four samples. Such an inversely proportional relation between  $\gamma$  and  $\epsilon$  holds for all other cases, except for Ga and BiGa which showed similar  $\gamma$ .

The presence of the sudden shift in the  $\gamma$ - $\epsilon$  curves is not predicted by Lippmann's theory of electrocapillarity, which states that the voltage-induced surface tension decrease should follow a parabolic law  $\gamma = \gamma_0 - \frac{1}{2}C \cdot \Delta V^2$ , where  $\gamma_0$  is the surface tension at the potential of zero charge,  $C$  is the charge capacitance of the surface electrical double layer, and  $\Delta V$  is the difference between the liquid metal surface potential  $\epsilon$  and its potential of zero charge. Such a deviation from the Lippmann theory at higher (less negative)  $\epsilon$ , e.g.,  $\epsilon > -1.25$  V, was attributed to the dominant electrochemical oxidation (over the electrocapillary effect) under such strong oxidizing conditions.<sup>[25]</sup> The surface oxide layer formed in an electrolyte is likely hydroxide in nature,<sup>[26]</sup> but these two oxide forms will not be differentiated in this study. The point that surface oxidation caused the deviation of the  $\gamma$ - $\epsilon$  relations of Ga-based liquid metals from Lippmann's theory was supported by the result obtained using liquid mercury (Hg),<sup>[27]</sup> in which the surface tension-potential curves are near parabolic and absent of a sudden shift, as Hg is not prone to electrochemical oxidation. The  $i$ - $t$  curves were further measured using an electrochemical station when they formed pendent droplets, which showed their stability for surface tension measurement (Figure S10, Supporting Information). It is notable that stable droplets could not be formed at voltages higher than those presented in Figure 3c. Instead, falling stream (wires) similar to those observed by Song et al. were formed (Figure S11, Supporting Information).<sup>[28]</sup>

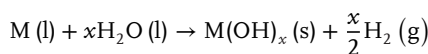
When an external voltage  $U$  was applied to a liquid metal in an electrolyte, its surface tension modulation by the electrochemical oxidation of the liquid metal was accompanied by the competing dissolution of the metal oxides ( $\text{Ga}_2\text{O}_3$ ,  $\text{SnO}$ ,  $\text{Bi}_2\text{O}_3$ , and  $\text{ZnO}$ ). As such, the observed fractal formation behaviors were the accumulative results of all these processes. Combining our surface tension measurements and observation of fractal formation, the results suggest that a voltage level sufficient to reduce the liquid metal surface tension was required to initiate fractal formation. This voltage level should correspond to  $U_{1,2}$ , below which non-branched droplets were observed (Figure S1, Supporting Information). Since  $U_{1,2} \geq 1.0$  V in all the liquid metal fractal experiments ( $c = 1.0$  mol  $\text{L}^{-1}$ ), the  $\epsilon$ - $U$  curves (Figure 3b) and  $\gamma$ - $\epsilon$  curves (Figure 3c) suggest that the surface tension of the liquid metals in all cases should decrease significantly under the applied voltage, given the close reference electrode potentials between the Cu

electrode (+0.34 V) and the Ag/AgCl electrode (+0.22 V) used in the two measurements.

The fractals were unstable and break up into fragments without a sufficiently thick oxide shell (small  $U$  or large  $c$ ). This happens when the oxide dissolves more quickly than it forms. In this case, the electrochemical reaction in the system mainly followed Equation (1), leading to the formation of solvated metal ion species.



where M represents different metal elements including Ga, Sn, Zn, and Bi.  $\text{H}_2$  was generated on the counter electrode. For the fractals to be stabilized, a higher voltage level in correspondence to  $U_{2,3}$  was needed to form an oxide layer that was stable and thick enough. At high  $U$  or low  $c$ , the electrochemical oxidation of the liquid metal alloys was dominated by formation of solid oxide species, following Equation (2). The existence of a thick oxide layer was evidenced by the color changes of the fractals observed in our experiment. We note that the processes taking place at the liquid metal interface are complicated in nature, which might not be fully described by Equations (1) and (2).



#### 2.4. Electrochemical Measurement of Liquid Metal Fractals

Given that the voltage-induced surface tension change and the formation/dissolution of surface oxides of the liquid metals were electrochemical in nature, cyclic voltammetry tests were carried out to gain more insights into the mechanism. During the tests, the NaOH concentration was kept at  $1.0$  mol  $\text{L}^{-1}$  and  $U$  was modulated at a scan rate were  $50$  mV  $\text{s}^{-1}$ . Depending on the liquid metal compositions and the fractal modes, different scan ranges of  $U$  were selected. In each case,  $U$  was increased gradually with a step size of  $0.2$  V to measure the current-voltage (CV) curves (Figure S12, Supporting Information).

As shown in Figure 4, the CV curves of all liquid metals fall into three categories: i) At low  $U$  levels (Figure 4a), the curves showed nearly linear current-voltage dependence during both the first forward (increasing  $U$ ) scan and the successive reverse (decreasing  $U$ ) scan. The current  $I$  during the forward and reverse scans was essentially the same, which indicated weak electrochemical oxidation and negligible oxide accumulation on the sample surface. Consequently, all samples behaved similarly as Ga-dominant conductive electrodes; ii) When  $U$  increased to higher values (Figure 4b), while the forward scan remained linear,  $I$  of the reverse scan became lower than that of the forward scan followed by a sharp drop to near zero. The hysteresis in the current intensity drops during the reverse scan indicated that significant solid oxide species could accumulate on the liquid metal surface, but the process was not instant, due to the counteracting oxide dissolution process. The resulting surface oxide layer suppressed the interfacial charge transport and led to the observed  $I$  decrease. The liquid metal fractals formed under these intermediate  $U$  conditions could not stabilize and eventually broke into

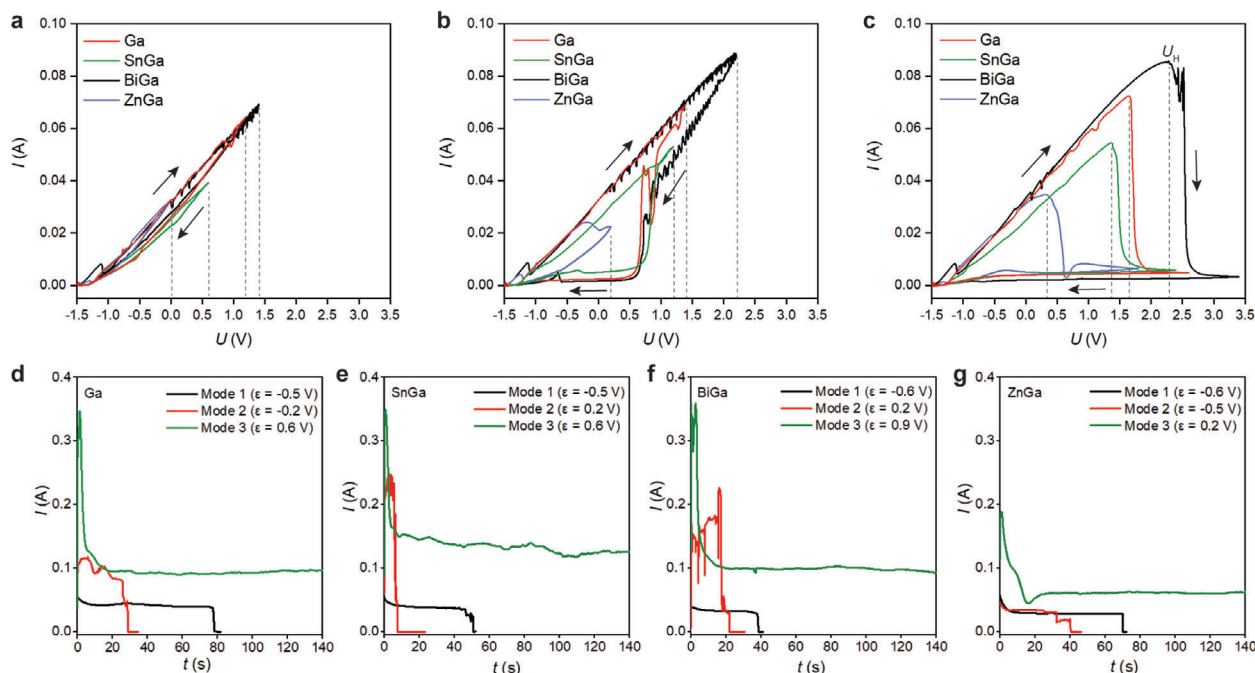


**Figure 4.** a–c) Comparison of CV curves at low  $U$  levels a), intermediate  $U$  levels b), and high  $U$  levels c) of the Ga, SnGa, BiGa, and ZnGa liquid metals. The arrows indicate scan directions. The turning point at which  $I$  started to drop was defined as  $U_H$ . Note that each liquid metal displayed a similar CV trend under a number of  $U$  values in our measurement (Figure S12, Supporting Information), and the curves featuring the largest  $U$  range (or equivalently, the highest  $U$  upper value) of each CV curve type were presented here. d–g) Current-time ( $i$ - $t$ ) curves of the three modes of Ga d), SnGa e), BiGa f), and ZnGa g). The volume of all the droplets were kept at 14  $\mu$ L.

smaller fragments due to their insufficiently strong surface oxide layer formation; iii) Further increasing  $U$  resulted in an abrupt  $I$  drop to near zero during the forward scans due to fast oxide layer thickening, and this minimum  $I$  remained during the following reverse scan (Figure 4c). In this case,  $U$  was sufficiently high for electrochemical oxidation to dominate the process against oxide dissolution in the forward scan, forming an oxide layer which greatly suppressed  $I$ . With the formation of a thick and persistent surface oxide layer, the fractals became stable.

Recalling the liquid metal fractal morphology diagrams (Figure 2), the three types of CV curves are indeed well matched by the three fractal formation modes. Note that the comparison here is qualitative as the fractal experiments ( $U$  fixed) and the CV measurement ( $U$  varied) were conducted under different conditions. Particularly, during the forward scan at high  $U$  levels (Figure 4c),  $I$  decreased sharply after  $U$  continuously increased to a certain point (referred to as  $U_H$ ) and the  $U_H$  of the four liquid metals followed the order ZnGa < SnGa < Ga < BiGa. This trend agreed reasonably with the observed fractal formation tendency of the different liquid metals. For example, the threshold voltage for stable fractal formation  $U_{2,3}$  revealed the order ZnGa < Ga < SnGa < BiGa (Table S1, Supporting Information). The difference in the sequence between Ga and SnGa was not considered to be a discrepancy as  $U_{2,3}$  of the two was very close (2.0 V for Ga and 2.1 V for SnGa, respectively), especially given that  $U_{2,3}$  was adjusted stepwise (step size 0.1 V) during our experiment. Nevertheless, both  $U_{2,3}$  and  $U_H$  implied that ZnGa and BiGa require, respectively, the lowest and the highest voltage to form stable fractals among all the liquid metals, which was a general trend observed in our experiment.

To obtain more insight into the oxidation process, we performed current-time measurement ( $i$ - $t$  curves) for the three fractal modes of the four types of liquid metal droplets (Figure 4d–g). Note that different voltages were used for different samples as they showed varied threshold voltages for transitioning between the three modes. In general, the four samples revealed similar  $i$ - $t$  curve trends in their respective modes, but different current densities, which again highlighted the influence of the secondary metals on the liquid metals' surface electrochemistry. In Mode 1, the four liquid metal droplets showed a similar trend that, after a slight drop within the first 20 s, the current remained steady until the droplets detached from the electrode (current then reached zero). In Mode 2, the current increased considerably in comparison to Mode 1, but eventually dropped to zero after the droplets detached from the electrode. Between the application of the voltage and the detachment of the liquid metal droplets, Mode 2 showed considerable current fluctuations (in particular for BiGa) and took less time than Mode 1 for the droplet-electrode detachment to occur. Both results indicated the unstable nature of the liquid metal droplets in this Mode. When it comes to Mode 3, the current further increased (with a sharp decrease at the beginning), after which the current became overall stable and persistent for over 2 min, as a result of the surface formed oxide layer stabilizing the fractals. This implied that surface electrochemical processes (e.g., oxidation, oxide dissolution, other ion/charge transport) were occurring in a dynamical equilibrium when stable fractals were formed.

All our observations and measurements show that the addition of a secondary metal, even a small amount, significantly alters the electrocapillary and electrochemical processes of these liquid

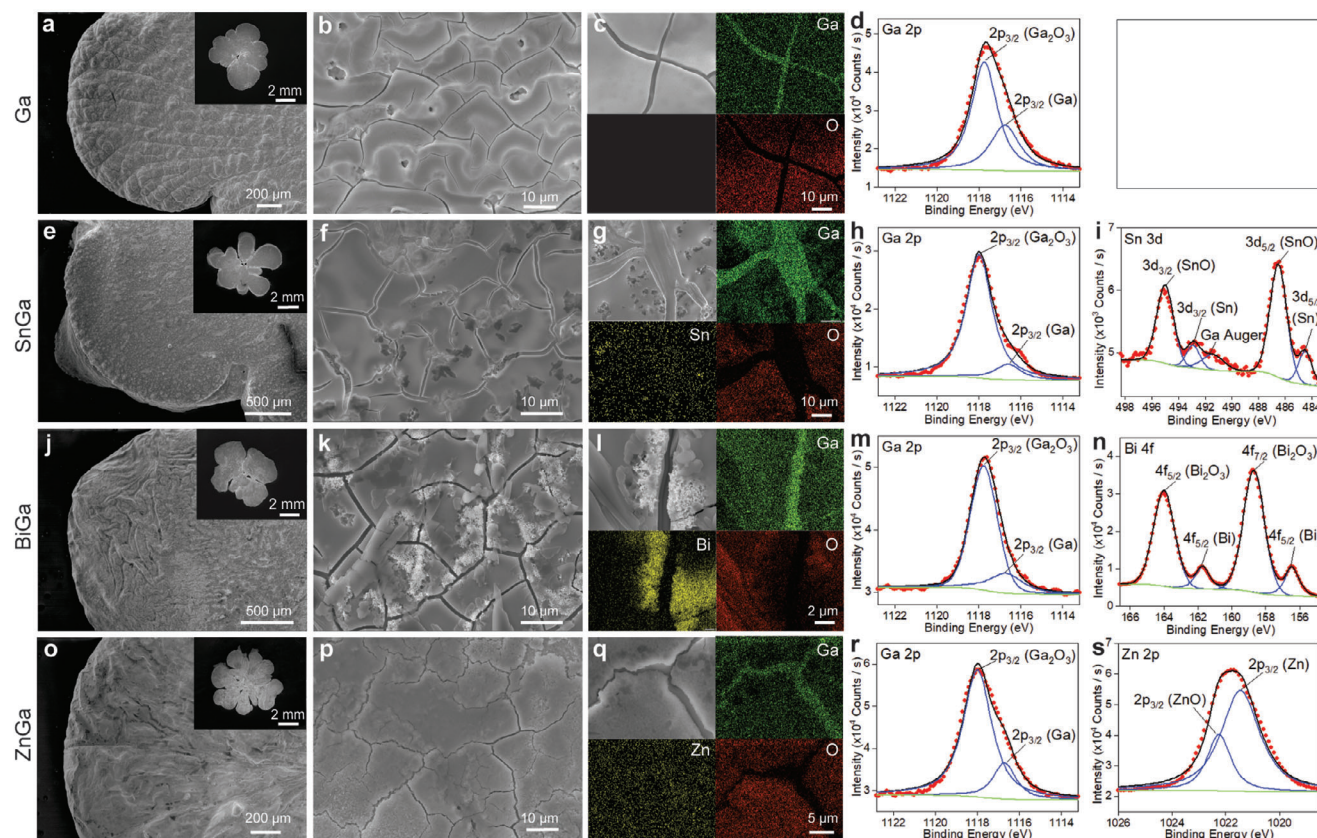


**Figure 5.** a–s) Surface morphology and composition analyses of solidified fractals (washed with water). SEM images of solidified fractals of Ga a,b), SnGa e,f), BiGa j,k), and ZnGa o,p) at different magnifications. EDS analysis of solidified fractal surfaces of Ga c), SnGa g), BiGa l), and ZnGa q). XPS spectra of solidified fractal surfaces of Ga d), SnGa h,i), BiGa m,n), and ZnGa r,s).

metals, resulting in distinct fractal formation behaviors. The effect of these minor alloy components could be related to their electrode potential relative to that of the solvent Ga. As shown in Table S2 (Supporting Information), the standard electrode potential  $E^0$  of the metals Ga ( $E^0 = -0.5490$  V), Sn ( $E^0 = -0.1375$  V), Bi ( $E^0 = 0.3080$  V), and Zn ( $E^0 = -0.7628$  V) followed the order of Zn < Ga < Sn < Bi. As a more negative  $E^0$  indicates that the metal is more susceptible to oxidation, it is expected that adding Zn, Sn, Bi to Ga could shift the tendency of the resulting liquid metals to form stable fractals according to the above  $E^0$  order, thus leading to the  $U_{2,3}$  order ZnGa < Ga < SnGa < BiGa. It should be noted that the relative ratio of different metals in the liquid binary alloys can also influence the oxidation processes. Since all these alloys consist of Ga primarily, the formation of Ga oxide is expected, while the co-existence of other oxide species is possible. The compositions of the surface oxides will be measured and discussed in the next section.

## 2.5. Fractal Surface Characterization

The surface compositions and morphologies of the stable fractals of different liquid metals were further characterized combining scanning electron microscopy (SEM), energy dispersive X-ray spectroscopy (EDS) and X-ray photoelectron spectroscopy

(XPS). The analyses were only conducted on stable fractals since only they could be transferred after solidification (using a Peltier cooler) without largely damaging the surface.

As shown in Figure 5, the fractal samples washed by water all had wrinkled surfaces that were covered by surface oxides. The oxide layers featured a thickness at hundred-nanometer level, and the introduction of the secondary metals were found to increase the oxide layer thickness according to our XPS depth profile analyses (Figures S13 and S14, Supporting Information). Cracked surface morphology was formed when the samples were solidified and dried. At the crack sites, the major component Ga was detected underneath the oxide layer. Bismuth metal was observed to appear at the edges of the cracks in the BiGa sample (Figure 5l). The XPS spectra revealed that the surface oxides from all fractal samples contain  $\text{Ga}_2\text{O}_3$ , due to the high Ga ratio in the liquid metals. Apart from  $\text{Ga}_2\text{O}_3$ , oxides of the minor components, namely SnO,  $\text{Bi}_2\text{O}_3$ , and ZnO, were also detected on the surface of BiGa, SnGa, and ZnGa, respectively. The oxidation of both the secondary (Sn, Bi, or Zn) and primary (Ga) metals was able to take place in each alloy since the applied voltages were typically higher than the oxidation potential of both. The difference in solubility between the metal oxides ZnO,  $\text{Ga}_2\text{O}_3$ , SnO, and  $\text{Bi}_2\text{O}_3$  (Table S3, Supporting Information) also contributed to the diversified fractal formation behaviors. However, considering that all samples formed the same  $\text{Ga}_2\text{O}_3$ , together with the oxide of the

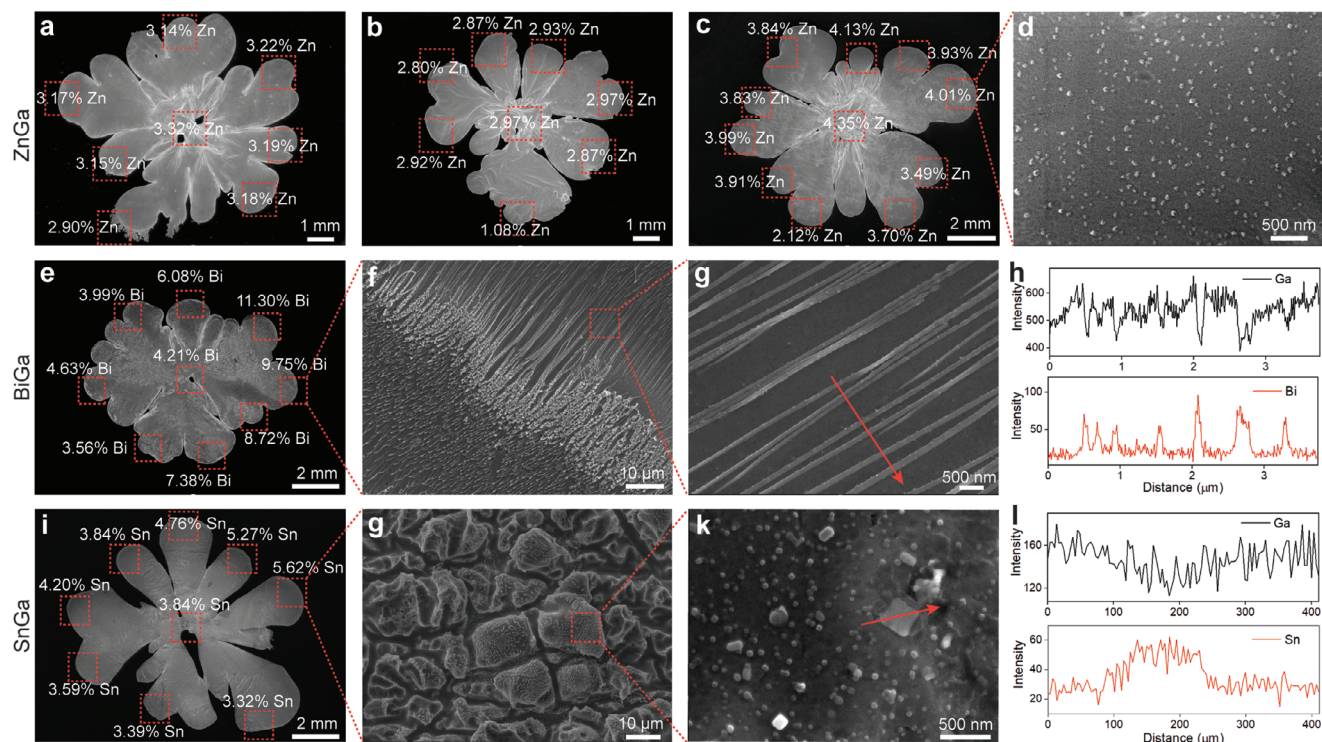


**Figure 6.** The distribution of secondary metals in the solidified fractals with surface oxide removed by HCl washing. a–c) SEM images of three ZnGa fractal samples with their normalized (to Zn and Ga) Zn wt% at the central and boarder locations indicated. d) Magnified region of c) showing the surface morphology of the ZnGa sample. e–g) SEM images of a BiGa fractal at different magnifications with its normalized (to Bi and Ga) Bi wt% at the central and boarder locations indicated. h) EDS line scan of the separated surface Bi patterns. i–k) SEM images of a SnGa fractal at different magnifications with its normalized (to Sn and Ga) Sn wt% at the central and boarder locations indicated. l) EDS line scan of the separated surface Sn structures.

secondary metals for the alloys, we suggest that the influence of oxide dissolution is not as strong as the electrochemical oxide formation. Specific to the ZnGa, Zn is more susceptible to oxidation than Ga while ZnO is more soluble than Ga<sub>2</sub>O<sub>3</sub> (Table S3, Supporting Information). The former explains the formation of stable fractals at lower voltages than other cases. Despite its high solubility, a considerable amount of ZnO (judging from ZnO XPS intensity) co-existed with Ga<sub>2</sub>O<sub>3</sub> on the ZnGa surface, indicating significant oxidation of Zn in the alloy.

Different metals in liquid alloys are mixed at the atomic scale and these freely moving atom species can diffuse among each other. Further given the differences in their atomic structure and properties, we suspect different metals respond differently to an external electric field, resulting in a non-uniform distribution of the two metals when the fractals form. To test this hypothesis, we solidified the liquid metals samples after stable fractals formed while maintaining the applied voltage, so that the element distribution induced by the electric field could be spatially locked locally after the voltage was terminated. The solidified fractal samples were washed with 0.1 mol L<sup>-1</sup> HCl solution to eliminate the contribution from surface oxides. The ratios of the secondary metals were determined by SEM and qualitative EDS (detection depth ≈ 1 μm).

As shown in Figure 6a–c, in the case of ZnGa, the Zn ratio at the center region of the HCl-washed (oxide removed) fractals was indeed >12% (average) higher than that of the edge areas,

and such a center-enriched Zn distribution was observed across three ZnGa samples. Since during fractal formation the anode is inserted at the fractal center, it appeared that Zn tended to accumulate toward higher electrical potentials, presumably due to the different ion mobility of the different metals in a liquid state and under an electric field gradient. However, for SnGa and BiGa, there was no apparent compositional difference of the secondary element across the fractals, but the secondary elements were found to enrich on the surface. This was evidenced by the much higher surface Bi ratio (average 6.9 wt%) (Figure 6e–g; Figure S15, Supporting Information) and surface Sn ratio (average 4.9 wt%) (Figure 6i–k; Figure S15, Supporting Information) of the solidified fractals than the nominal ratio of Bi (0.3 wt%) and Sn (1.7 wt%). In comparison, the measured Zn ratios (average 3.8 wt%) on the solidified ZnGa fractal surface were comparable with its starting ratio (3.9 wt%). The surface enrichment of the secondary metal in the BiGa and SnGa fractals was also evidenced by the formation of surface phase separated Bi and Sn structures, with distinct morphologies (Figure 6e–h, i–l). These observations agree with our previous report.<sup>[23,29]</sup> Surface phase separation was not observed in the ZnGa fractals (Figure S16, Supporting Information), noting that particulate features were found on the surface of both ZnGa and Ga fractals (Figure 6d; Figure S15, Supporting Information). Control samples prepared without applying an external voltage were further analyzed which revealed uniform distribution of the secondary elements across

the samples (Figure S17, Supporting Information), and validated the hypothesis that the applied electric field was the main factor that drove Zn to accumulate at the center region of the fractal samples. We suspect that for the BiGa case, the element distribution induced by surface enrichment due to solidification<sup>[29]</sup> is much stronger than that caused by the electric field during fractal formation (Figure S17b, Supporting Information). Therefore, due to the strong influence of surface phase enrichment during solidification, we are unable to rule out possible electric-field-induced element redistribution in the BiGa case.

### 3. Conclusion

In summary, we explored how minor metal components influenced the interfacial electrocapillary and electrochemical activities of liquid metal alloys by investigating their fractal formation behaviors. Three Ga-based binary liquid alloys with dilute secondary element inclusions, namely SnGa, BiGa, and ZnGa were employed and compared with Ga. The fractal formation behaviors of all the investigated liquid metals were categorized into three modes, namely “nonbranched droplets”, “unstable fractals”, and “stable fractals”, as the applied positive DC voltage was progressively increased. Interestingly, different liquid metal systems showed distinct voltages settings for transitions between different modes. A comprehensive set of experiments including surface tension measurements, electrochemical CV measurements, composition, and morphology analyses were carried out to identify the underlying mechanisms. It was found that the fractal formation was governed by the voltage-induced surface tension change of the liquid metals, the electrochemical surface oxide formation, and the competing oxide dissolution process. A deviation of the  $\gamma$ - $\epsilon$  (surface tension-surface potential) curves away from Lippmann’s equation was observed, which was indicative of the dominance of electrochemical oxidation under the strong oxidizing conditions. The existence of minor alloy components including Sn, Bi, and Zn in the Ga solvent affected all these surface processes, thereby resulting in their different fractal morphologies. In addition, evidence was found that an external electric field could induce nonuniform spatial distributions of solute elements in the liquid metal fractals of ZnGa.

Surface tension modulation and shape transformation of liquid metals are important for their applications in microfluidics, reconfigurable electronics and liquid/soft robotics, while the control over their surface electrochemistry, particularly surface element distribution, is critical for developing liquid metal-based catalysis and sensing systems. The discovery that the electrocapillarity and electrochemistry of liquid metals can be controlled by introducing a small amount of a secondary metal offers a feasible path for designing liquid metals with precisely tuned properties. This, in turn, is anticipated to significantly broaden the range of applications for liquid metals.

### 4. Experimental Section

**Materials and Liquid Alloy Preparation:** The Ga (99.999%, round shot, Zi (99.99%, shot, Sigma-Aldrich), Bi (99.99%, chunk, Rotometals), and Sn (99.9%, popcorn, Rotometals) were used as received for source alloy preparation. A milligram balance (ENTRIS641-1S, Sartorius Lab Instru-

ments) was used for measuring the weight of the metals. To prepare the liquid alloys ( $\text{Zn}_{3.9}\text{Ga}_{96.1}$ ,  $\text{Sn}_{1.7}\text{Ga}_{98.3}$ ,  $\text{Bi}_{0.3}\text{Ga}_{99.7}$ ), pre-weighed metal precursors were added in glass vials and allowed to melt on a hotplate (Thermoline Scientific) with temperatures above the melting point of individual metals. The weight ratios of the metals were chosen so that the melting point of the resulting alloys is close to room temperature. A glass rod was used to stir sufficiently the molten metals to ensure homogeneous mixing. These liquid metal samples were stored in an oven with the temperature kept at 50 °C for later use. The sodium hydroxide (NaOH) (pellets, Chem-Supply) and hydrochloric acid (HCl) (32%, RCL Labscan) were used to prepare the solutions. Milli-Q water (18.2 M $\Omega$  cm) and ethanol (100% undenatured, Chem-Supply) were used in all experiments.

**Liquid Metal Fractal Formation and Observations:** In a typical experiment, a fresh liquid metal droplet of fixed volume (14  $\mu\text{L}$ ) was transferred using a pipette into a glass Petri dish (30 mm in diameter) which is pre-filled with NaOH solution ( $\approx 3$  mL). A DC power supply (SPD3303X, SIGLENT Technologies) was used to apply a positive voltage from 1.0 to 2.6 volt to the liquid metal droplets. The liquid metal droplet was connected to the power supply by a tungsten tip (100  $\mu\text{m}$  in diameter) as the anode. A copper ring cathode was used to obtain a radial electric field distribution. A digital camera was utilized to record the shape deformation of the liquid metal droplet induced by the applied voltages. The experiment was carried out at a constant temperature of 30 °C, controlled by a Peltier module (33 W/4 A). To obtain solidified fractals, the samples were cooled down inside the Petri dish (without terminating the electric field). The solidified fractal samples were washed with either water or HCl solution for further characterization.

**Material Characterization:** The SEM and EDS characterizations were implemented by an analytical SEM system (JSM-IT500HR, JEOL). The X-ray photoelectron spectroscopy (XPS) and depth profile analysis were performed by high-resolution XPS (ESCALAB250Xi, Thermo Scientific) using a monochromatic Al K alpha soft X-ray source (486.68 eV), with a power of 120 W (13.8 kV  $\times$  8.7 mA), a spot size of 500  $\mu\text{m}$ , a photoelectron take-off angle of 90°. The data was analyzed using the Avantage software and the C1s binding energy (284.8 eV) was referenced. It was noted that the surface of the fractals was not microscopically flat due to the wrinkles generated during fractal formation (Figure 5), which could bring complexity in interpreting the XPS depth profiles. To minimize the influence of the surface morphology, uniform and visually “flat” surface regions (2.5 mm  $\times$  2.5 mm) were carefully selected and etched in the XPS measurement. A reference etching rate of 0.18 nm s<sup>-1</sup> was used for converting the etching time into etching depth in Figures S13 and S14 (Supporting Information). The depth profile in Figure S13 (Supporting Information) was plotted based on the XPS spectra in Figure S14 (Supporting Information).

**Surface Tension Measurement:** The pendant drop method was conducted with a three-electrode system to measure the surface tension of the liquid metals used in this study. The liquid metal was kept into a 1 ml syringe and the latter was fixed onto a syringe pump (Fusion 200, Chemyx Inc.) to precisely ( $< \pm 0.35\%$ ) control the amount of liquid metal extruded at a rate of 0.2 mL min<sup>-1</sup> to control the droplet size. The liquid metal droplet was immersed in 1.0 mol L<sup>-1</sup> NaOH solution. A positive voltage  $U$  was applied between the working electrode (liquid metal pendant drop) and the counter electrode (a gold coil) with the DC power supply, and the corresponding voltage  $\epsilon$  between the working electrode and an Ag/AgCl reference electrode (reference potential +0.22 V, CH Instruments, Inc.) was measured with a digital multimeter (SDM3065X, SIGLENT Technologies). The voltage  $U$  was gradually increased from 0 to different terminal voltages based on the liquid metals used, with an interval of 0.1 V, and a digital microscope (CELESTRON) was used for taking photos of the shape of the liquid metal droplet after the shape was stabilized. An image analysis software OpenDrop was used to calculate the surface tension based on the droplet shape captured.<sup>[30]</sup> All experiments were conducted on the hotplate at 30 °C.

**Electrochemical Measurement:** The electrochemical measurement was performed in a three-electrode cell using a CHI650E electrochemical workstation (CH Instruments, Inc.). A liquid metal droplet with a volume of 14  $\mu\text{L}$ , the same to that used in the liquid metal fractal experiment, was immersed in 1.0 mol L<sup>-1</sup> NaOH solution. The droplet was held using a

plastic vial with its top surface exposing to the solution and its bottom was connected to the electrochemical workstation by a copper wire. The copper wire in contact with the NaOH solution was insulated, and thus has no charge transport with the solution during the experiment. The CV curves were obtained at a scan rate of  $50 \text{ mV s}^{-1}$  and a sensitivity of  $10 \text{ mV s}^{-1}$ . The  $i-t$  curves in Figure 4d–g were obtained at a sample interval of 0.05 s and a sensitive of  $0.1 \text{ A V}^{-1}$ . The OCP of all the liquid metals were measured to be close to  $-1.6 \text{ V}$  versus Ag/AgCl. The OCP was measured at a sample interval of 0.1 V and a run time of 400 s, before measuring CV and  $i-t$  curves (Figure S9, Supporting Information). The electrochemical measurements of the four samples were measured in  $1.0 \text{ mol L}^{-1}$  NaOH solution. All experiments were conducted at  $30 \text{ }^\circ\text{C}$  to avoid the solidification of the liquid metals.

## Supporting Information

Supporting Information is available from the Wiley Online Library or from the author.

## Acknowledgements

This work was supported by the Australian Research Council (ARC) Discovery Early Career Researcher Award (DE220100816), the ARC Centres of Excellence FLEET (CE170100039), and the ARC Laureate Fellowship grant (FL180100053).

Open access publishing facilitated by University of New South Wales, as part of the Wiley - University of New South Wales agreement via the Council of Australian University Librarians.

## Conflict of Interest

The authors declare no conflict of interest.

## Data Availability Statement

The data that support the findings of this study are available in the supplementary material of this article.

## Keywords

electrocapillary, electrochemical oxidation, fractal modes, liquid metals, surface tension

Received: February 6, 2023

Revised: April 22, 2023

Published online:

- [1] a) T. Daeneke, K. Khoshmanesh, N. Mahmood, I. A. De Castro, D. Esrafilzadeh, S. J. Barrow, M. D. Dickey, K. Kalantar-Zadeh, *Chem. Soc. Rev.* **2018**, *47*, 4073; b) Q. Wang, Y. Yu, J. Liu, *Adv. Eng. Mater.* **2018**, *20*, 1700781; c) K. Kalantar-Zadeh, J. Tang, T. Daeneke, A. P. O'Mullane, L. A. Stewart, J. Liu, C. Majidi, R. S. Ruoff, P. S. Weiss, M. D. Dickey, *ACS Nano* **2019**, *13*, 7388.
- [2] a) K. Kalantar-Zadeh, M. A. Rahim, J. Tang, *Acc. Mater. Res.* **2021**, *2*, 577; b) L. Ren, X. Xu, Y. Du, K. Kalantar-Zadeh, S. X. Dou, *Mater. Today* **2020**, *34*, 92.
- [3] Y. He, J. Tang, K. Kalantar-Zadeh, M. D. Dickey, X. Wang, *Proc. Natl. Acad. Sci. USA* **2022**, *119*, 2117535119.
- [4] a) K. Khoshmanesh, S.-Y. Tang, J. Y. Zhu, S. Schaefer, A. Mitchell, K. Kalantar-Zadeh, M. D. Dickey, *Lab Chip* **2017**, *17*, 974; b) S. J. Dacuycuy, W. A. Shiroma, A. T. Ohta, *Micromachines* **2022**, *13*, 572.
- [5] a) M. D. Dickey, *Adv. Mater.* **2017**, *29*, 1606425; b) A. B. M. T. Haque, R. Tutika, R. L. Byrum, M. D. Bartlett, *Adv. Funct. Mater.* **2020**, *30*, 2000832.
- [6] J. Zhang, Y. Yao, L. Sheng, J. Liu, *Adv. Mater.* **2015**, *27*, 2648.
- [7] M. A. Rahim, J. Tang, A. J. Christofferson, P. V. Kumar, N. Meftahi, F. Centurion, Z. Cao, J. Tang, M. Baharfar, M. Mayyas, F.-M. Allieux, P. Koshy, T. Daeneke, C. F. McConville, R. B. Kaner, S. P. Russo, K. Kalantar-Zadeh, *Nat. Chem.* **2022**, *14*, 935.
- [8] X. Wang, W. Yao, R. Guo, X. Yang, J. Tang, J. Zhang, W. Gao, V. Timchenko, J. Liu, *Adv. Healthcare Mater.* **2018**, *7*, 1800318.
- [9] S. C. Hardy, *J. Cryst. Growth* **1985**, *71*, 602.
- [10] a) C. B. Eaker, M. D. Dickey, *Appl. Phys. Rev.* **2016**, *3*, 031103; b) X. Zhao, S. Xu, J. Liu, *Front. Energy* **2017**, *11*, 535.
- [11] a) J. Zhang, L. Sheng, J. Liu, *Sci. Rep.* **2014**, *4*, 7116; b) M. R. Khan, C. B. Eaker, E. F. Bowden, M. D. Dickey, *Proc. Natl. Acad. Sci. USA* **2014**, *111*, 14047; c) F. F. Yun, Z. Yu, Y. He, L. Jiang, Z. Wang, H. Gu, X. Wang, *Natl. Sci. Rev.* **2019**, *7*, 366.
- [12] a) S.-Y. Tang, V. Sivan, K. Khoshmanesh, A. P. O'Mullane, X. Tang, B. Gol, N. Eshtiaghi, F. Lieder, P. Petersen, A. Mitchell, *Nanoscale* **2013**, *5*, 5949; b) S.-Y. Tang, K. Khoshmanesh, V. Sivan, P. Petersen, A. P. O'Mullane, D. Abbott, A. Mitchell, K. Kalantar-zadeh, *Proc. Natl. Acad. Sci. USA* **2014**, *111*, 3304; c) J. Tang, X. Zhao, Y. Zhou, J. Liu, *Adv. Mater. Interfaces* **2017**, *4*, 1700939.
- [13] J. Han, M. Mayyas, J. Tang, M. Mousavi, S. A. Idrus-Saidi, S. Cai, Z. Cao, Y. Wang, J. Tang, R. Jalili, A. P. O'Mullane, R. B. Kaner, K. Khoshmanesh, K. Kalantar-Zadeh, *Matter* **2021**, *4*, 4022.
- [14] a) J. Wissman, M. D. Dickey, C. Majidi, *Adv. Sci.* **2017**, *4*, 1700169; b) A. Zavabeti, T. Daeneke, A. F. Chrimes, A. P. O'Mullane, J. Zhen Ou, A. Mitchell, K. Khoshmanesh, K. Kalantar-zadeh, *Nat. Commun.* **2016**, *7*, 12402.
- [15] M. U. Baig, K. S. Elassy, A. Høst-Madsen, A. T. Ohta, W. A. Shiroma, A. Nosratinia, *EURASIP J. Wireless Commun. Networking* **2021**, *2021*, 158.
- [16] a) M. Mayyas, M. Mousavi, M. B. Ghasemian, R. Abbasi, H. Li, M. J. Christoe, J. Han, Y. Wang, C. Zhang, M. A. Rahim, J. Tang, J. Yang, D. Esrafilzadeh, R. Jalili, F.-M. Allieux, A. P. O'Mullane, K. Kalantar-Zadeh, *ACS Nano* **2020**, *14*, 14070; b) S. A. Idrus-Saidi, J. Tang, S. Lambie, J. Han, M. Mayyas, M. B. Ghasemian, F.-M. Allieux, S. Cai, P. Koshy, P. Mostaghimi, K. G. Steenbergen, A. S. Barnard, T. Daeneke, N. Gaston, K. Kalantar-Zadeh, *Science* **2022**, *378*, 1118; c) A. Zavabeti, J. Z. Ou, B. J. Carey, N. Syed, R. Orrell-Trigg, E. L. H. Mayes, C. Xu, O. Kavehei, A. P. O'Mullane, R. B. Kaner, K. Kalantar-zadeh, T. Daeneke, *Science* **2017**, *358*, 332.
- [17] L. Chen, E. Bonaccorso, *Adv. Colloid Interface Sci.* **2014**, *210*, 2.
- [18] S. Troian, X. Wu, S. A. Safran, *Phys. Rev. Lett.* **1989**, *62*, 1496.
- [19] I. Bischofberger, R. Ramachandran, S. R. Nagel, *Nat. Commun.* **2014**, *5*, 5265.
- [20] a) Z. W. Yu, Y. C. Chen, F. F. Yun, X. L. Wang, *Adv. Eng. Mater.* **2017**, *19*, 1700190; b) S. Chen, L. Wang, Q. Zhang, J. Liu, *Sci. Bull.* **2018**, *63*, 1513; c) C. B. Eaker, D. C. Hight, J. D. O'Regan, M. D. Dickey, K. E. Daniels, *Phys. Rev. Lett.* **2017**, *119*, 174502.
- [21] M. B. Ghasemian, A. Zavabeti, M. Mousavi, B. J. Murdoch, A. J. Christofferson, N. Meftahi, J. Tang, J. Han, R. Jalili, F. M. Allieux, M. Mayyas, Z. Chen, A. Elbourne, C. F. McConville, S. P. Russo, S. Ringer, K. Kalantar-Zadeh, *Adv. Mater.* **2021**, *33*, 2104793.
- [22] Y. Ding, M. Zeng, L. Fu, *Matter* **2020**, *3*, 1477.
- [23] J. Tang, S. Lambie, N. Meftahi, A. J. Christofferson, J. Yang, J. Han, M. A. Rahim, M. Mayyas, M. B. Ghasemian, F.-M. Allieux, Z. Cao, T. Daeneke, C. F. McConville, K. G. Steenbergen, R. B. Kaner, S. P. Russo, N. Gaston, K. Kalantar-Zadeh, *Nat. Synth.* **2022**, *1*, 158.

- [24] A. R. Jacob, D. P. Parekh, M. D. Dickey, L. C. Hsiao, *Langmuir* **2019**, *35*, 11774.
- [25] R. S. Perkins, *J. Electrochem. Soc.* **1972**, *119*, 713.
- [26] M. Song, K. E. Daniels, A. Kiani, S. Rashid-Nadimi, M. D. Dickey, *Adv. Intell. Syst.* **2021**, *3*, 2100024.
- [27] D. C. Grahame, R. P. Larsen, M. A. Poth, *J. Am. Chem. Soc.* **1949**, *71*, 2978.
- [28] M. Song, K. Kartawira, K. D. Hillaire, C. Li, C. B. Eaker, A. Kiani, K. E. Daniels, M. D. Dickey, *Proc. Natl. Acad. Sci. USA* **2020**, *117*, 19026.
- [29] J. Tang, S. Lambie, N. Meftahi, A. J. Christofferson, J. Yang, M. B. Ghasemian, J. Han, F.-M. Allieux, M. A. Rahim, M. Mayyas, T. Daeneke, C. F. McConville, K. G. Steenbergen, R. B. Kaner, S. P. Russo, N. Gaston, K. Kalantar-Zadeh, *Nat. Nanotechnol.* **2021**, *16*, 431.
- [30] E. Huang, A. Skoufis, T. Denning, J. Qi, R. R. Dagastine, R. F. Tabor, J. D. Berry, *J. Open Source Software* **2021**, *6*, 2604.